Geophysical Research Letters

Supporting Information for

Earthquake fingerprint of an incipient subduction of a bathymetric high

Luigi Passarelli[1,2, †,*], Simone Cesca[3], Nima Nooshiri[4], Sigurjón Jónsson[1]

1 King Abdullah University of Science and Technology (KAUST), Thuwal, 23955-6900, Saudi Arabia
2 Swiss Seismological Service, ETH-Zürich, Sonneggstrasse 5, 8092 Zürich, Switzerland
3 GFZ German Research Centre for Geosciences, Telegrafenberg, 14473 Potsdam, Germany
4 DIAS Dublin Institute for Advanced Studies, 10 Burlington Rd, Dublin, D04 C932,
* luigi.passarelli@ingv.it ORCID 0000-0001-8995-8765
† current address: Istituto Nazionale di Geofisica e Vulcanologia, sezione di Bologna, Via Franceschini 31, 40128 Bologna

Contents of this file

S1. Focal Mechanism inversion waveform similarity

Moment tensor inversions were performed modeling full waveforms and their amplitude spectra, following the approach described in Cesca et al. 2010. We used regional recordings from seismic broadband stations located at distances up to 2000 km. Data and metadata from open seismic stations can be accessed using IRIS, Orfeus and GEOFON web services. Contributing seismic stations pertain to the following networks: AU (Australian National Seismograph Network), G (GEOSCOPE; IPGP and EOST, 1982), II (Global Seismograph Network – IRIS/IDA; Scripps Institution of Oceanography, 1986), IU (Global Seismograph Network – IRIS/USGS; Albuquerque Seismological Laboratory/USGS, 1988), ND (New Caledonia Broadband Seismic Network; Centre IRD de Noumea, 2010), NZ (New Zealand National Seismograph Network; http://info.geonet.org.nz/display/equip/New+Zealand+National+Seismograph+Network), S1 (Australian Seismometers in Schools; http://ausis.edu.au/). Given that ray paths travel along large distances, synthetic seismograms were computed for a simplified, average velocity model with a homogeneous velocity crust (v_P 6 km/s, v_S 3.46 km/s, thickness 15 km) above a global mantle model (AK135). We chose variable ranges of epicentral distances and frequency bands for the inversion, based on the original magnitude estimate from global seismic catalogs (Tab. S1). Moment tensor (MT) solutions were directly computed for 177 earthquakes for a pure double-couple model. Focal mechanisms were then classified applying a DBSCAN clustering algorithm (Cesca, 2020) using the similarity of the focal mechanisms, i.e., the Kagan angle, as metric. The results are illustrated in Figure S3.

We extended the moment tensor analysis indirectly to the complete dataset of 777 earthquakes, including the 177 events for which we already had MT solutions (which we refer to as master events). Here we scanned the earthquakes with no direct MT solution (target events), and compared their waveforms recorded at selected stations (360 s long vertical displacements at stations AU.NFK. and G.DZM.00, filtered between 0.02 and 0.05 Hz (Fig 1 inset)) with those of the 177 master events. Whenever we found cross-correlations for both stations above 0.9, we interpreted the high waveform similarity to attest a similarity of locations and focal mechanisms. In such cases, we assigned to the target event the focal mechanism of the master event with the most similar waveform. Using this approach, focal mechanisms were estimated for 618 earthquakes. Applying again the focal mechanism clustering (Cesca, 2020), we could confirm that the vast majority of the earthquakes were normal faulting events (Figure S4).

Magnitude	Bandpass [Hz]	Max Epic. Dist. [km]
M > 7.00	0.010-0.025	2000
M 5.75-7.00	0.010-0.030	1200
M 5.25-5.75	0.015-0.040	1200
M < 5.25	0.018-0.050	1200

Table S1. Selection of bandpass filter and maximal epicentral distance, based on the original estimate of the earthquake magnitude, for the MT inversion.

S2 Source specific term correction

The data set consists of the arrival times of first *P* and first *S* waves of 610 earthquakes included in the USGS-ANSS bulletin. The seismic events occurred between late October 2017 and late February 2019 and were recorded by both regional and global seismic stations. Nearly all arrival time picks had been revised and picked manually by USGS analysts. The objective of the source-specific station terms (SSST) method is to reduce the effect of spatially correlated residuals caused by the 3-D velocity structure (Nooshiri et al., 2017). By using this technique, we iteratively computed a set of station corrections for each receiver. Therefore, the time corrections for each station vary as a function of seismic source position. We solved the spherical forward problem of calculating travel times of *P*- and *S*-wave arrivals by assuming the global 1-D earth model ak135. The station corrections are thus relative to the 1-D reference model ak135. Rather than using the hypocenters in the USGS catalogue as starting locations for our relocation procedure, we relocated all of the events with the NonLinLoc program. However, poor seismic network coverage at regional distances and strong effects of the local topography hindered satisfactorily improvement in the relocation procedure.

S3 Cumulative slip calculation in Fig. 3 main text

Cumulative seismic slip was calculated using moment-rupture area scaling (Thingbaijam et al., 2017) for normal and thrust earthquakes, assuming seismogenic depths of 10 km and dip 15° for the slab and 20 km and dip of 70° for the outer-rise normal faults. This results in fault width of ~20 km and ~40 km for normal and thrust earthquakes, respectively. A rigidity of 30 GPa was used. Cumulative slip was calculated in 0.5 km bins along trench parallel direction as the average value of slip of 1000 Monte Carlo simulations of earthquake epicenters drawn from a Gaussian distribution $N(\mu_e,\sigma_e)$, where μ_e is the determined epicenter location and σ_e =5 km the standard deviation.

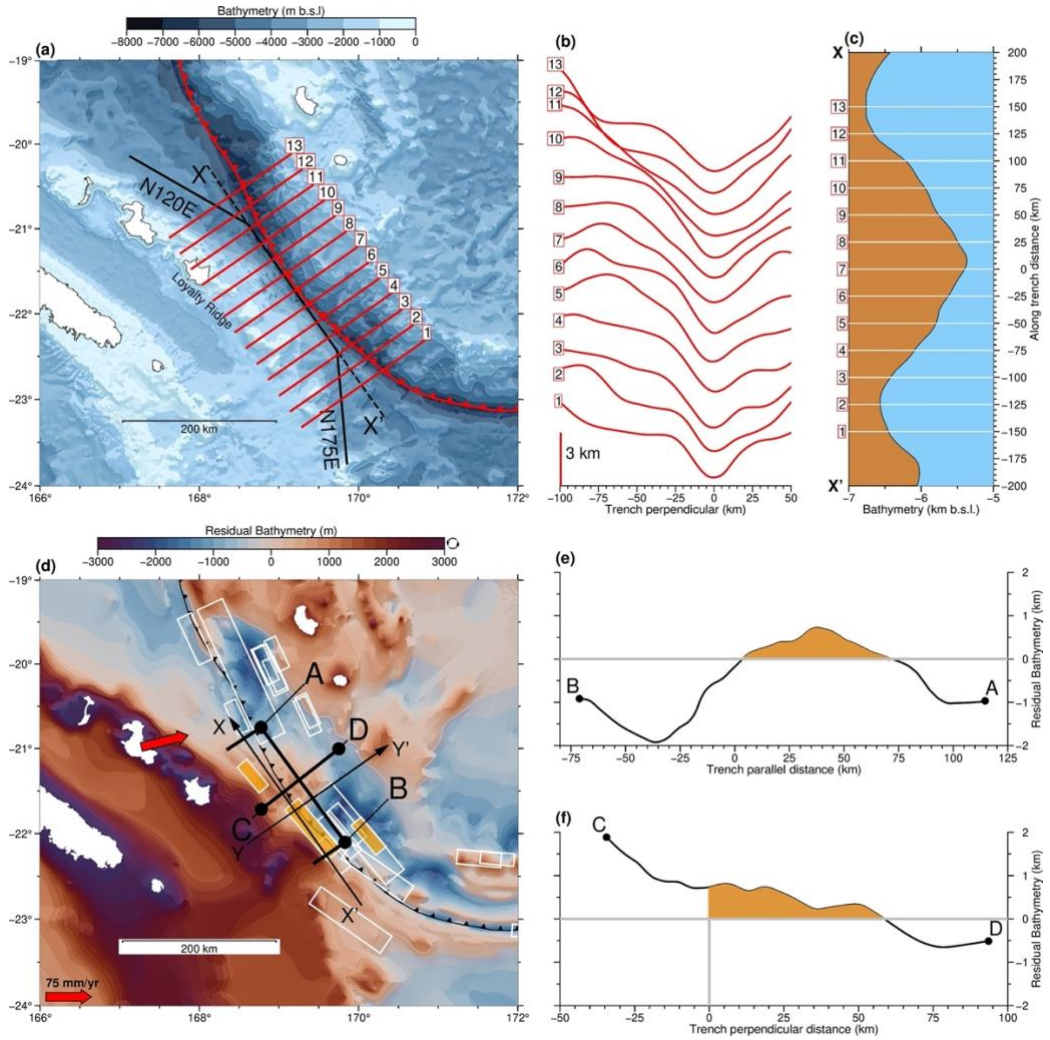

Figure S1. Bathymetric map and profiles across and along the Loyalty Ridge (LR) and Vanuatu Trench (VT). a) Bathymetric map from SRTM30plus (see main for reference), with the red line indicating the VT and thick black lines the main trends of LR. Numbered trench-perpendicular profiles are oriented N55°E with 25 km spacing (shown in panel **b**) and profile X-X′ represents the same coordinate axis as in Fig. 2 main text. **b)** Bathymetry along trench-perpendicular profiles (location in panel a), averaged on sliding disks of 12.5 km radius every 2 km of trench-perpendicular distance and centered at the trench. **c)** Bathymetric profile along trench for the segment marked by X-X′ as in the same Cartesian coordinate system of Fig. 2 of the main text. **d)** Residual bathymetry map as after the analysis of Bassett and Watt (2015). White rectangles are earthquakes with $M_w \geq 7$ with oranges shaded rectangles are of this study as in Fig. 1 main text. Trench perpendicular short segments are LR-VT collision zone as in Fig.1. A-B and C-D segments are used in panels (e) and (f) to calculate the bathymetry profile in the X′X and YY′ Cartesian system (see Fig. 2 main text). **e)** Trench parallel residual bathymetric profile along A-B where shaded areas highlights the high anomaly. **f)** Trench perpendicular residual bathymetric profile along C-D where the shaded area highlights the high anomaly.

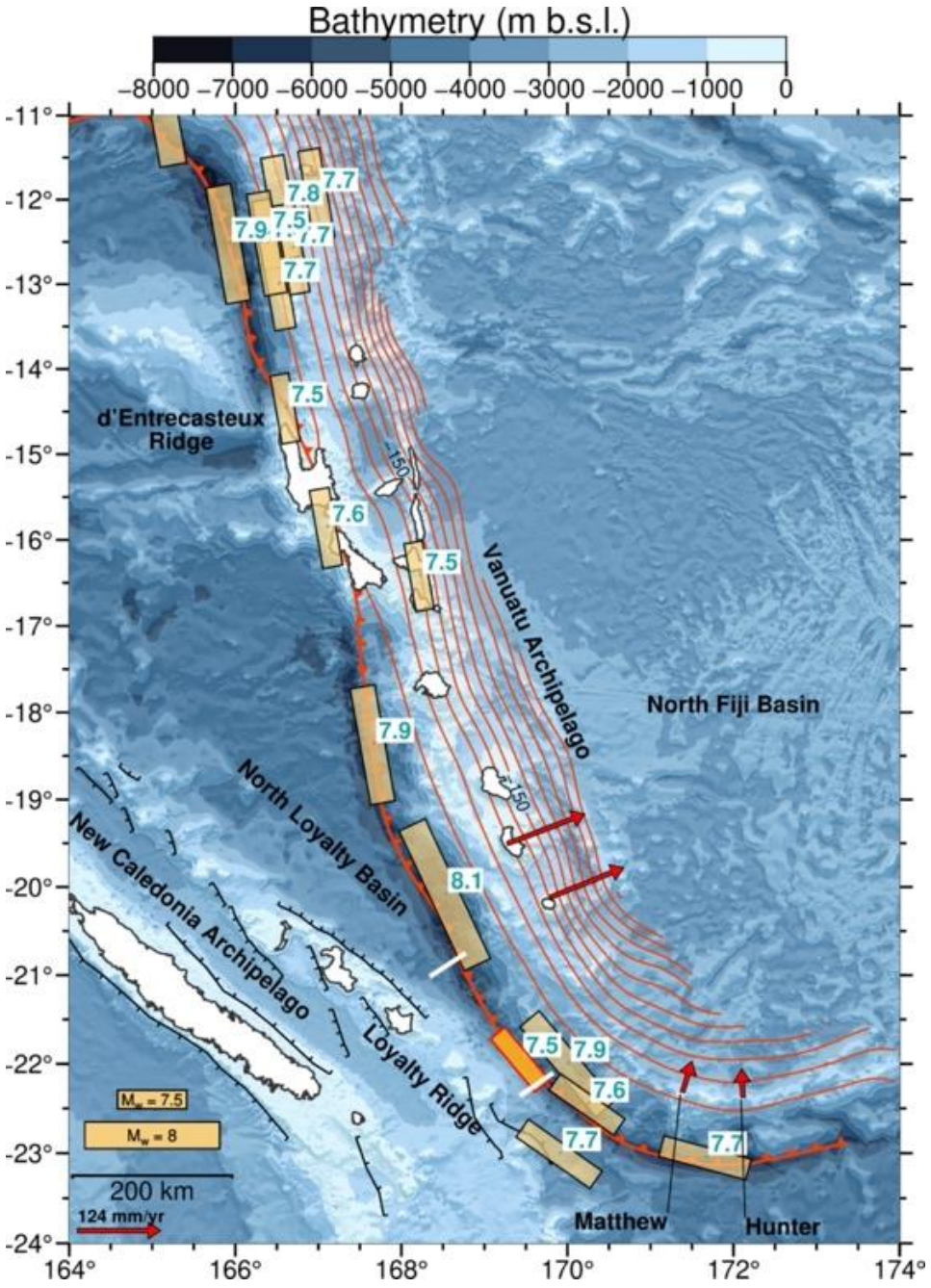

Figure S2. Seismicity map from 1900 to 2019. Same as Fig. 1 main text, except only for all Vanuatu subduction zone and large megathrust with $M_w \geq 7.5$. Labelled numbers are magnitude M_w of earthquakes.

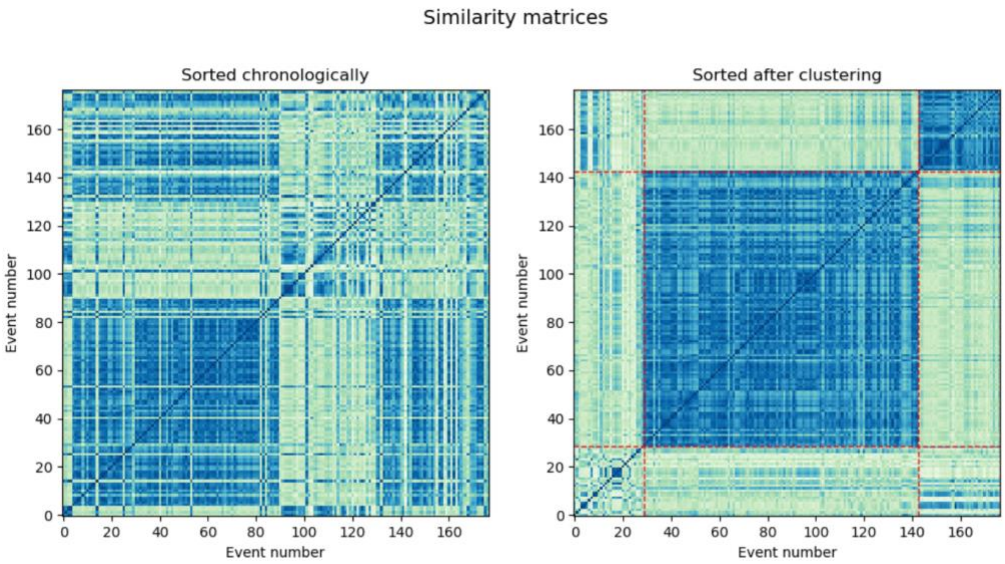

Figure S3. Similarity matrices for event Focal Mechanisms (FMs). Distance matrices comparing the 177 focal mechanism solutions determined in this study, sorted chronologically (left) and after clustering (right). A blue-to-white palette corresponds to small (white) to large (blue) difference (similarity) between focal mechanisms. The focal mechanism difference was computed by a normalized Kagan angle (Kagan 1991, 1992, Cesca 2020). After the clustering, we identified three groups of events (left to right, separated by dashed red lines): First, a very small group of somewhat dissimilar earthquakes (with variable focal mechanisms), a second large cluster of normal faulting earthquakes, and then the third smaller cluster of thrust faulting earthquakes).

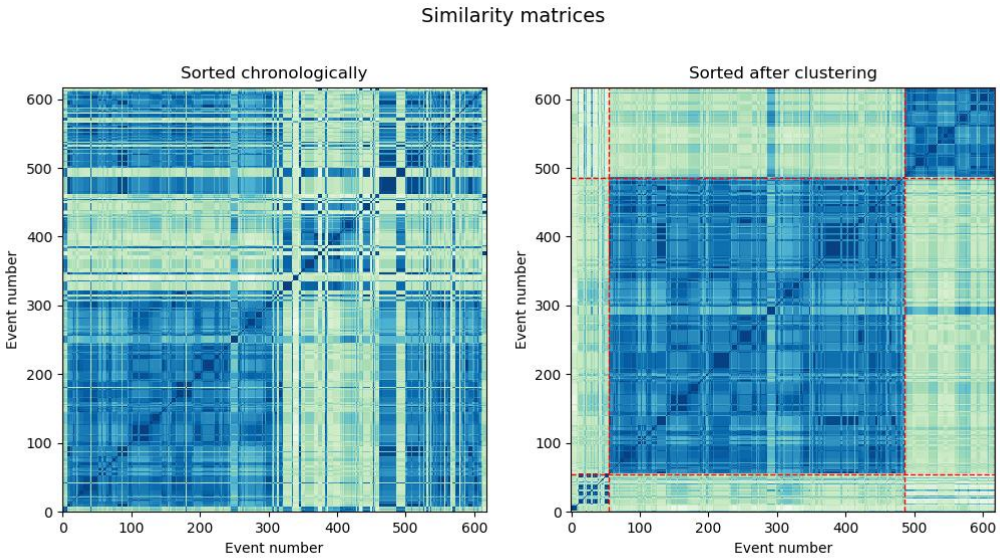

Figure S4. Same as S3, except for than 618 focal mechanism solutions obtained in this study either based on moment tensor inversions (177 events) or from existing focal mechanisms with most similar waveforms, using vertical components at stations AU.NFK. NS G.DZM.00. See main text, Fig.1 and text S1 for explanation of the method.

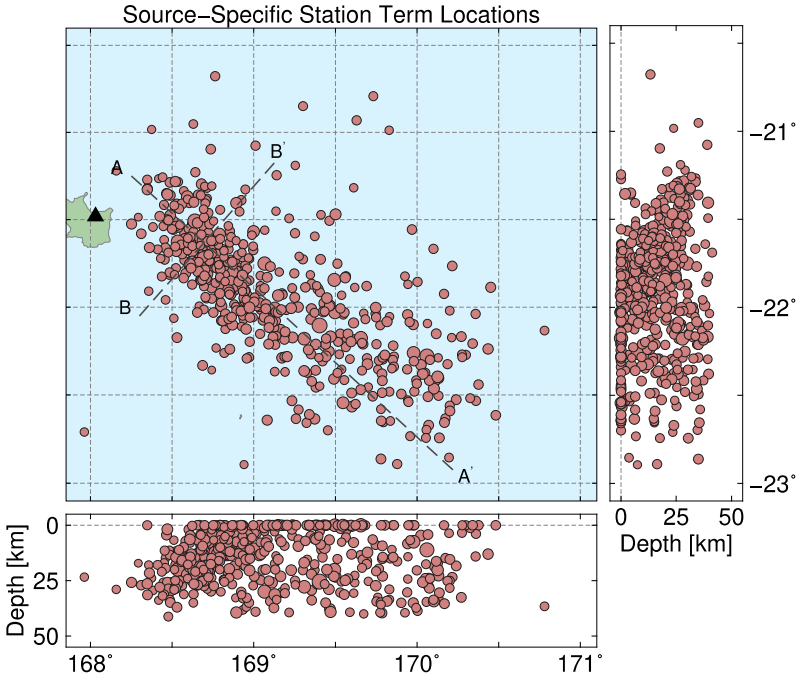

Figure S5. Relocated earthquakes by using the source-specific station terms (SSST) method. See text in the supplement for explanation of the text S2.

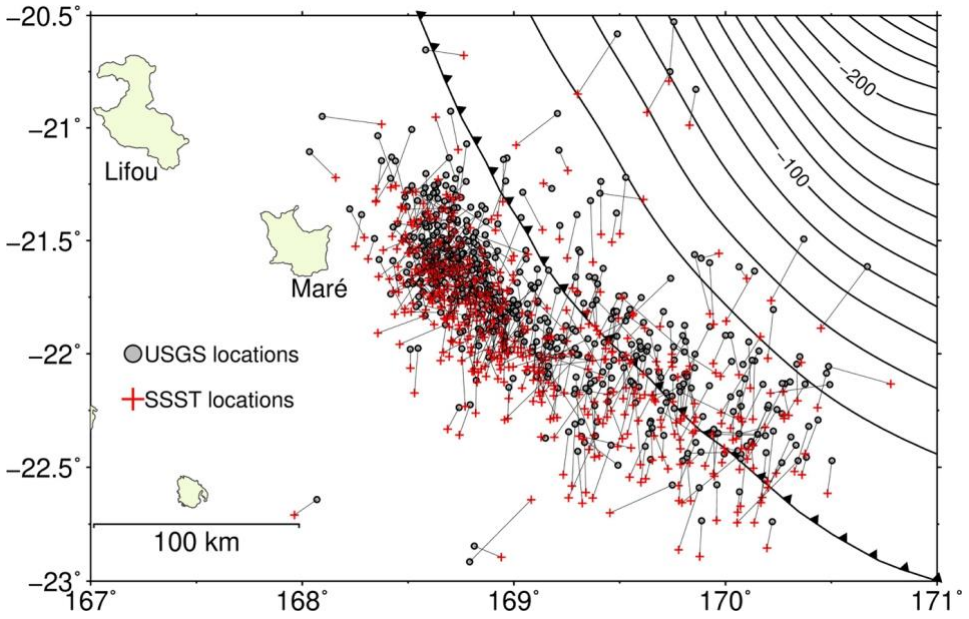

Figure S6. Difference between ANSS locations and the relocated events shown in Fig. S5. USGS-ANSS epicenters are indicated as USGS locations in the figure legend. SSST stands for source-specific station terms method discussed in the supplementary text and presented in Fig. S5.

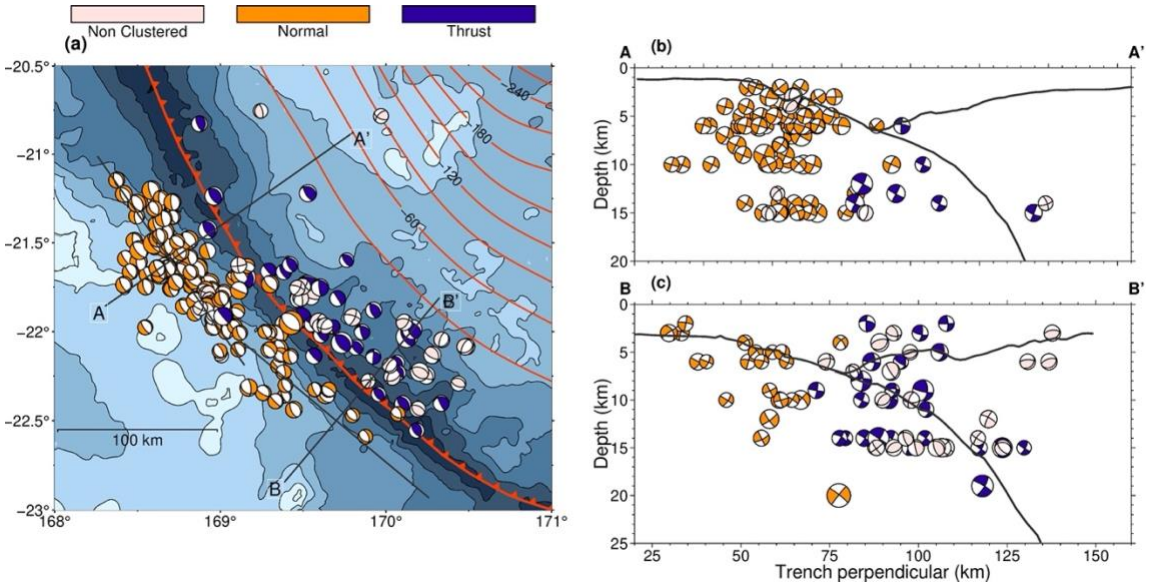

Figure S7. FMs in map view and two cross sections. a) The FMs of this study mapped using centroid locations, with profiles A-A′ and B-B′ indicating the cross sections shown in panels **b)** and **c)**. Thick black lines in b) and c) are the bathymetric profile and slab interface along A-A′ and B-B′. Slab model is Slab2.0 (Hayes 2018) and please note that x-axis and y-axis are not in the same scale. Please note that depth of FMs refer to sea level and is not corrected for bathymetric profile.

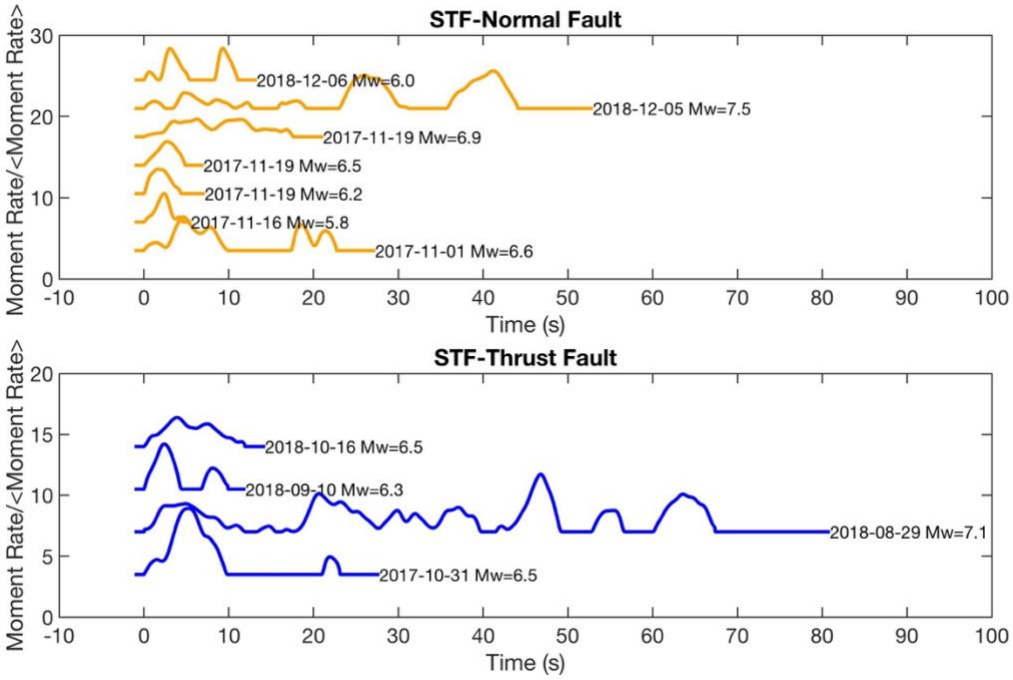

Figure S8. Source-time function from the SCARDEC database. Each source-time function (STF) is normalized by the mean and shifted by 1.5 log-point for plotting purposes. The top panel shows STFs for normal faulting earthquakes in 2017-2018 along the LR, while the bottom panel STFs for thrust faulting events in 2017-2018 along the NH interface. The color code is the same as Fig. 2. SCARDEC is an open database of STFs and moment magnitude reported here are from this database (Vallee et al., 2011).

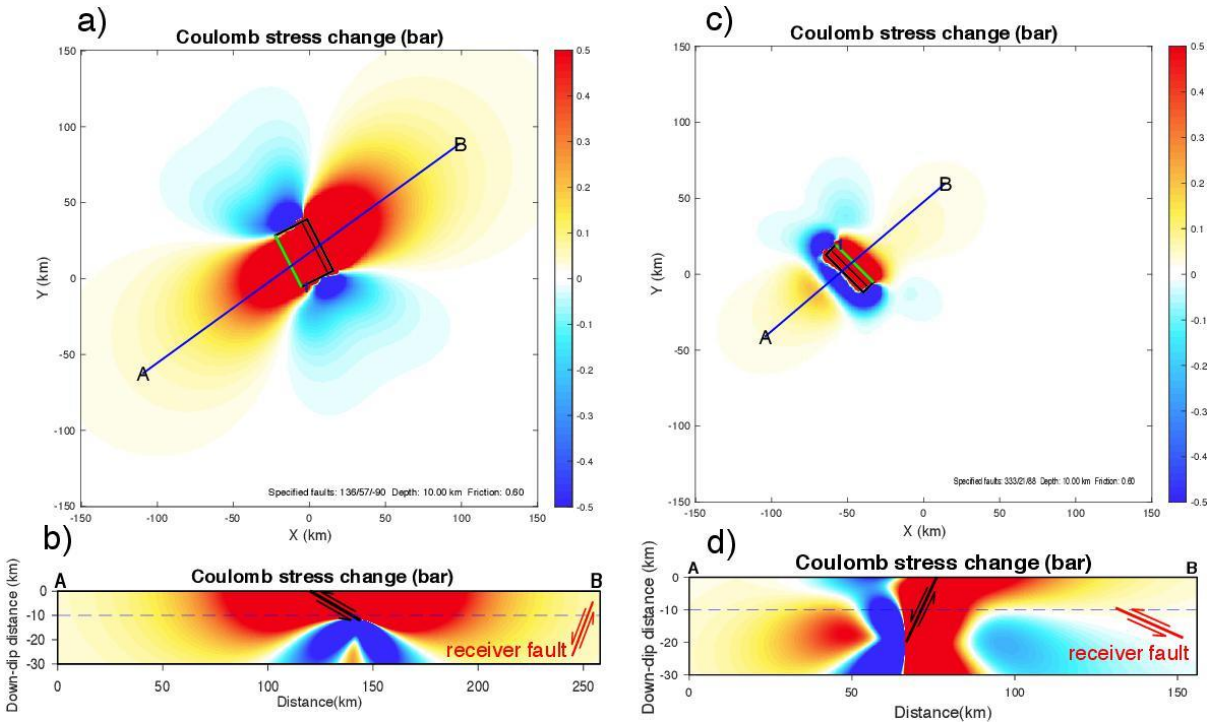

Figure S9. Coulomb Failure Stress changes ΔCFS. Panels a) and b) show a map view and cross section along A-B of ΔCFS due to the Mw6.8 thrust earthquake of 31 October 2017 onto the Mw6.7 normal fault, which slipped on 1 November 2017 (receiver fault). Green and black lines in panel a) are fault strike and depth of 10 km for the map view as indicated by dashed line in panel b). In panel b) the source and receiver faults are indicated in black and red respectively. Panels c) and d) are the same as a) and b), but for the Mw7.5 normal earthquake on 5 December 2018 onto the fault of the Mw6.7 thrust aftershock (receiver fault), which occurred later that same day. Both causative faults (sources) have planes reaching the surface as both earthquakes generated a tsunami. Fault parameters, depth of the map view, and the friction coefficient are reported at the bottom of the map. Color palette is in bar (0.1MPa) and saturated between -0.5 bar and 0.5 bar.

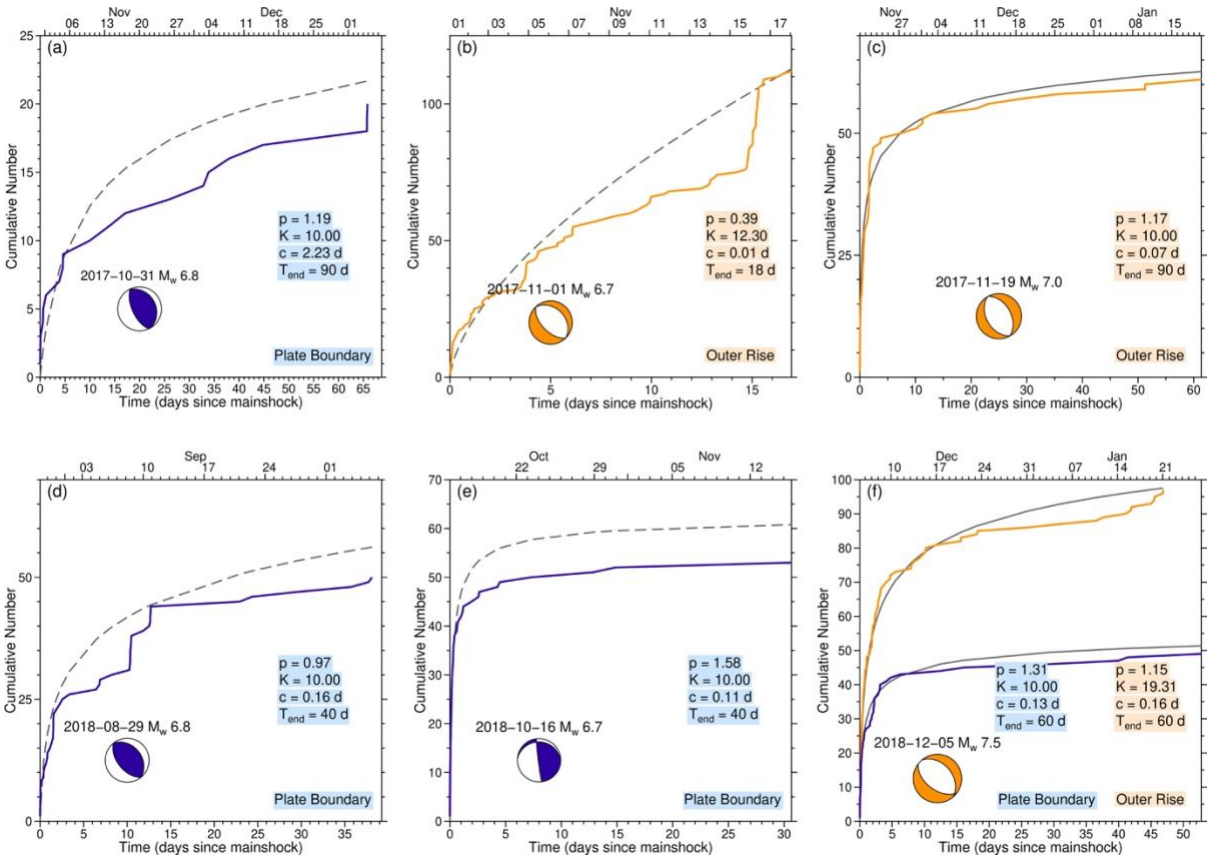

Figure S10. Omori-Utsu model fit for the largest events in the sequence. In panels a) to f), the mainshock is indicated with a beach-ball, date and magnitude, color-coded as in Fig. 2, where blue defines thrust faulting events and orange defines normal faulting events. Smooth curves show cumulative number of events from the Omori-Utsu model (fit parameters are given in legends, dashed curves indicate poor fits), while step-wise curves are observed cumulative number of aftershocks. In panel f) the curves represent aftershocks along the LR (outer rise) and at the plate boundary.

Reference

Bassett, D., & Watts, A. B. (2015). Gravity anomalies, crustal structure, and seismicity at subduction zones: 1. Seafloor roughness and subducting relief. *Geochemistry, Geophysics, Geosystems*, *16*(5). https://doi.org/10.1002/2014GC005684

Cesca, S. (2020): Seiscloud, a tool for density-based seismicity clustering and visualization, *J. Seismol.* 24,3, 443-457, https://doi.org/10.1007/s10950-020-09921-8

Hayes, G., 2018, Slab2 - A Comprehensive Subduction Zone Geometry Model. https://doi.org/10.5066/F7PV6JNV.

Nooshiri, N., Saul, J., Heimann, S., Tilmann, F., & Dahm, T. (2017). Revision of earthquake hypocentre locations in global bulletin data sets using source-specific station terms. *Geophysical Journal International*, *208*(2). https://doi.org/10.1093/gji/ggw405.

Thingbaijam, K. K. S., Mai, P. M., & Goda, K. (2017). New empirical earthquake source-scaling laws. *Bull. Seism. Soc. Am.*, *107*(5), 2225–2246. https://doi.org/10.1785/0120170017

Vallée, M., Charléty, J., Ferreira, A. M. G., Delouis, B., & Vergoz, J. (2011). SCARDEC: A new technique for the rapid determination of seismic moment magnitude, focal mechanism and source time functions for large earthquakes using body-wave deconvolution. *Geophys. J. Int.*, *184*(1). https://doi.org/10.1111/j.1365-246X.2010.04836.x